UNCLASSIFIED

Defense Technical Information Center
Compilation Part Notice

ADP011810

TITLE: Synthesis and Characterization of Nanocomposite Coatings

DISTRIBUTION: Approved for public release, distribution unlimited

This paper is part of the following report:

TITLE: NATO Advanced Research Workshop on Nanostructured Films and Coatings. Series 3. High Technology - Volume 78

To order the complete compilation report, use: ADA399041

The component part is provided here to allow users access to individually authored sections of proceedings, annals, symposia, etc. However, the component should be considered within the context of the overall compilation report and not as a stand-alone technical report.

The following component part numbers comprise the compilation report:
ADP011800 thru ADP011832

UNCLASSIFIED

SYNTHESIS AND CHARACTERIZATION OF NANOCOMPOSITE COATINGS

J. HE, M. ICE, AND E. J. LAVERNIA
Department of Chemical and Biochemical Engineering and Materials Science, University of California Irvine, Irvine, CA 92697-2575

Abstract

The synthesis of nanocomposite coatings is described in this paper. The nanocomposite feedstock powders are synthesized using mechanical milling, and the characteristics of the milled powders, i.e., morphology, agglomeration behavior, powder size, grain size and structural evolution during milling, are analyzed using X-ray diffraction, SEM and TEM. Using high velocity oxygen fuel (HVOF) spraying, the nanocomposite coatings are sprayed, and the microstructures and properties of the resulting coatings are characterized.

1. Introduction

In thermal spraying technology, molten or semi-molten powders are deposited onto a substrate to produce a two-dimensional coating or in some cases, a three-dimensional self-standing material. The microstructure and properties of the material depend on the thermal and momentum characteristics of the impinging particulate [1], which are determined by the spraying methodology and the type of feedstock materials employed. Powders, rods and wires can be used as feedstock materials. Metals and alloys in the form of rods or wires are commonly used in arc spraying (AS) and flame spraying (FS). Powders of metals, alloys, ceramic oxides, and cements are often employed in thermal spraying to form a homogeneous microstructure in the resulting coatings. In most cases, the sprayed surface should be degreased, masked and roughened prior to spraying to maximize the bonding strength between the coating and the substrate material. Various techniques for pre-spraying treatment have been described [2]. Today, a number of thermal spraying techniques are available. Flame spraying (FS), arc spraying (AS), detonation gun spraying (DGS), continuous detonation spraying (CDS), atmospheric plasma spraying (APS), twin wire arc spraying (TWAS), low pressure plasma spraying (LPPS) or vacuum plasma spraying (VPS), controlled atmosphere plasma spraying (CAPS), high velocity flame spraying (HVFS) and high velocity oxygen fuel spraying (HVOF) are widely used to produce various coatings for different industrial applications. The process and parameters of the spraying techniques mentioned above are summarized in Refs [1, 3]. HVOF spraying is the most significant development in thermal spraying industry since the development of plasma spraying [1] and it has been the topic of many

G.M. Chow et al. (eds.), Nanostructured Films and Coatings, 131–148.
© 2000 *Kluwer Academic Publishers. Printed in the Netherlands.*

excellent investigations in the recent past years [4-6]. HVOF is characterized by high particle velocity and low thermal energy when compared to plasma spraying. The applications of HVOF have expanded from the initial use of tungsten carbide coatings to include different coatings that provide for wear or erosion/corrosion resistance [7]. HVOF uses an internal combustion jet fuel (propylene, acetylene, propane, and hydrogen gases) to generate hypersonic gas velocities of 1830 m/s. When burned in conjunction with pure oxygen, these fuels can produce a nominal gas temperature greater than 3029 K. The powder particles are injected axially into the jet gas, heated, and propelled toward the substrate. With the relatively low temperatures of the flame gas associated with the HVOF systems, superheating or vaporization of individual particles are often prevented [8]. Furthermore, the lower particle temperatures present lead to carbide coatings that exhibit less carbide loss than that of the plasma sprayed coatings. In essence, the advantages of HVOF process over conventional plasma spraying are higher coating bond strength, lower oxide content, and improved wear resistance due to a homogeneous distribution of carbides [9,10]. In recent work [11], it was reported that the velocity and temperature of the HVOF sprayed particle powders could be controlled independently.

Nanostructured materials are characterized by a microstructural length scale in the 1-100 nm regime [12]. More than 50 volume percent of atoms are associated with grain boundaries or interfacial boundaries when the grain is small enough, thus a significant amount of interfacial component between neighboring atoms associated with grain boundaries contributes to the physical properties of nanostructured materials [13]. Using nanostructured feedstock powders, thermal spraying has allowed researchers to generate coatings with higher hardness, strength and corrosion resistance than the corresponding conventional coatings [3, 14]. A number of techniques that are capable of producing nanostructured materials include gas condensation, mechanical alloying/milling, crystallization of amorphous alloys, chemical precipitation, spray conversion processing, vapor deposition, sputtering, electro-deposition, and sol-gel processing techniques [15]. Mechanical alloying/milling techniques have been used to produce large quantities of nanocrystalline materials for possible commercial use [15]. Mechanical alloying/milling is a high energy ball milling process, in which elemental or pre-alloyed powders are welded and fractured to produce metastable materials with controlled microstructures. Today, mechanical alloying/milling has been widely used to synthesize amorphous alloys, intermetallic compounds and nanocrystalline materials [16-18]. During mechanical milling, particle welding and fracturing result in severe plastic deformation. Using mechanical milling, Cr_3C_2-NiCr and WC-Co nanocomposites were successfully synthesized [19-21] in our laboratories.

The objective of this paper is to describe the complete synthesis history of a nanocomposite coating, consisting of the synthesis of nanocomposite using mechanical milling, characteristics of the milled powder, thermal spraying process and characterization of the resulting coatings.

2. Synthesis and characteristics of nanocomposte powder

Pre-alloyed Cr_3C_2-25(Ni20Cr) powders (Dialloy 3004, Sulzer Metco (US) Inc. with a nominal particle size of (-45+5.5) microns are chosen for this study. The powders are

immersed in Hexane [$H_3C(CH_2)_4CH_3$] and mechanically milled with a modified Szegvari attritor model B at a rate of 180 rpm for 20 hours in a stainless steel tank with stainless steel balls. The ball to powder mass ratio is 20:1. To monitor the synthesis process, samples are taken from the tank every two hours for SEM, X-ray and TEM examination. SEM analysis performs on a Philips XL 30 FEG microscope. X-ray diffraction measurements are carried out using a Siemens D5000 diffractometer equipped with a graphite monochromator using Mo Kα (λ=0.070923 nm) radiation. General scans with a step size of 0.01° and a step time of 1s are conducted for phase identification; and detailed scans with a step size of 0.01° and a step time of 5s are conducted for grain size measurements. The milled powders to be analyzed by TEM are dispersed in Methanol, deposited on carbon grid substrates, and TEM observation is performed using a Philips CM20 microscope operated at 200 keV.

2.1 MORPHOLOGY OF THE MILLED POWDER

Figure.1 (a) shows the morphology of as-received powder which consists of a Cr_3C_2 carbide phase and a Ni20Cr phase (a solution of 20% Cr in Ni). A small amount of the powder exhibits a spherical morphology while the remainder shows an irregular morphology with sharp facets. Figure. 1 (b) shows the result of X-ray (EDS) dot mapping of Ni. There is a high Ni in the regions where spherical particles appear. While almost no Ni appears at the sites where irregular-shaped particles are present. This indicates that the Ni20Cr phase shows a spherical morphology and Cr_3C_2 carbides are present in form of irregular-shaped particles. Figure 1 (c) and (d) shows the changes in the powder after milling 8 and 16 hours, respectively. In Figure 1(c) a large as-received powder particle is evident (see arrow) illustrating the morphology of the powders after 8 hours milling. X-ray

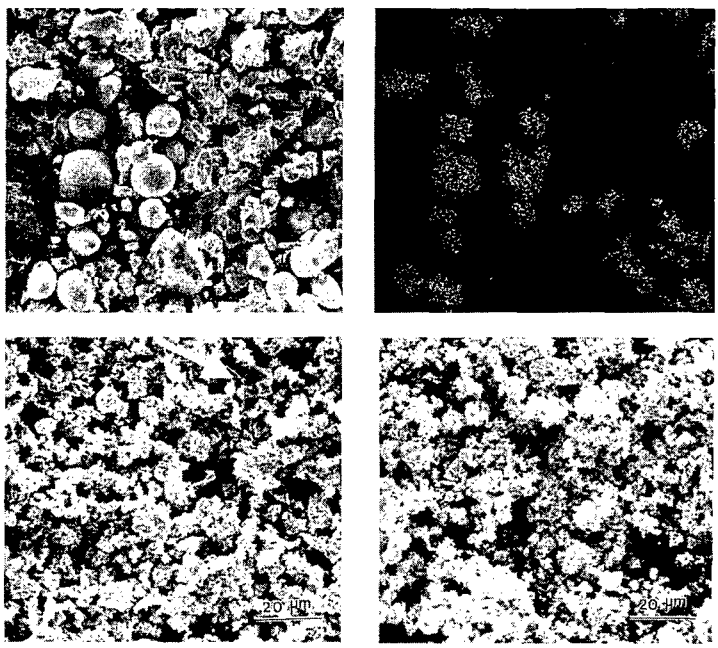

(c) (d)

Figure 1. Morphology of the powders following different milling times: (a) as-received powder; (b) Ni-map of (a); (c) 8 hour milled powder and (d) 16 hour milled powder.

mapping reveals that this particle, with sharp facets, is a carbide. This featured particle with sharp facets is not observed in the powder that is milled for 16 hours.

2.2 AGGLOMERATION BEHAVIOR AND AVERAGE SIZE OF MILLED POWDER

During mechanical milling, powder agglomeration is often observed. Two types of self-agglomeration behavior are observed in the present powder system, referred as binder-induced agglomeration and metallurgical agglomeration in this paper. Figure 2 shows SEM images illustrating binder-induced agglomeration. After 4 hours milling, see Figure 2(a), a large proportion of the small particles are self-agglomerated. However, the larger carbide particles, with sharp facets, remain non-agglomerated. A detailed view of the agglomerated powder, indicated by the arrow in Figure 2 (a), is shown in Figure 2(b). The presence of regular rectangular parallelepiped particles, indicated by arrows, is thought to be Cr_3C_2 carbides with an orthorhombic crystal structure that fracture along low Miller index planes, possibly {100} planes, during milling. X-ray dot mapping confirms that these particles are carbides. Figure 2 (c) shows almost complete self-agglomeration in the powder that has been milled for 20 hours. A magnification of the agglomerated powder indicated by the arrow in Figure 2(c) is shown in Figure 2 (d); X-ray mapping results indicate that the particles in Figure 2 (d) are neither pure carbide nor pure NiCr phase.

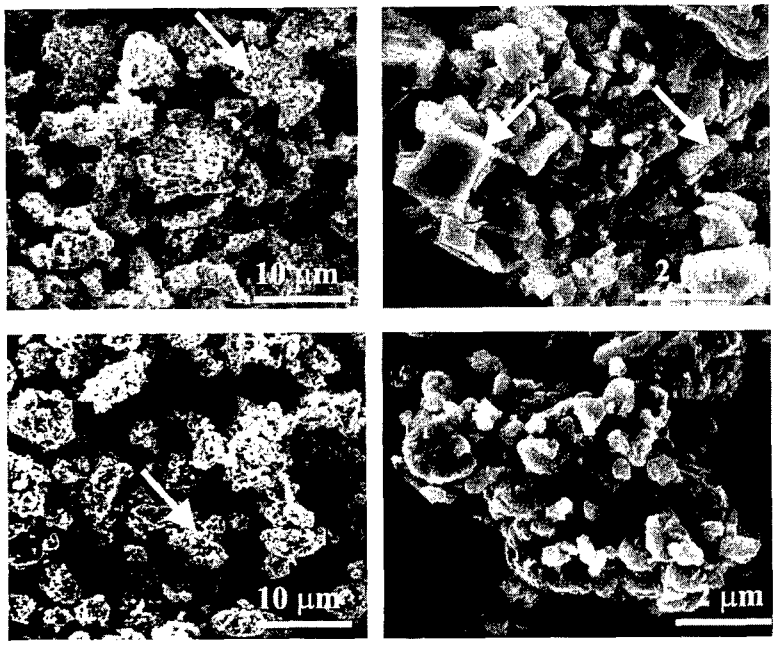

Figure 2. Morphology of the binder-induced self-agglomerated powders. (a) 4 hour milled powder; (b) magnification of (a); (c) 20 hour milled powder and (d) magnification of (c).

The self-agglomerated powders, shown in Figure 2, are not very dense, and referred as binder-induced agglomeration in this paper. The binder-induced agglomeration is primarily bonded by milling media, and can easily be decomposed back to its original powder form. For example, to make TEM samples, the powder is immersed into Methanol and vibrated by a supersonic instrument for a few minutes; under these

conditions, the agglomerates are broken down.

Figure 3 are TEM images illustrating the process of metallurgical agglomeration. An agglomerated powder is made of particles A, B, C and D. The SAD pattern on the interface of powders A and B is shown on the bright field image. This is a complex pattern of polycrystal diffraction rings and single crystal diffraction spots. On the side of powder A, the pattern comes from a polycrystal. A number of sharp carbide fragments can be observed. While, on the side of powder B, the pattern is essentially one of a f.c.c. single crystal. Similar complex SAD patterns are also diffracted on the interfaces of powder A with C, and A with D. Therefore, powder A is a polycrystal nanocomposite, and powder B, C and D are essentially single crystal NiCr solid solutions that are embedded with a few fragments of carbide particles. The interface of powders A and B is completely continuous and without microcracks or microvoids. The continuous and smooth interfaces between the powder particles in the agglomerates provide direct evidence that mechanical milling promotes metallurgical bonds between ductile NiCr solid solution materials and polycrystal composite powders. The self-agglomerated powder in Figure 3 is characterized by the metallurgical bond between the powders, and referred to as metallurgical agglomeration in this paper. The self-agglomeration process is primarily controlled by cold welding and fracturing that occurs during the milling process, and can not easily be decomposed because of the presence of metallurgical bonds between powders.

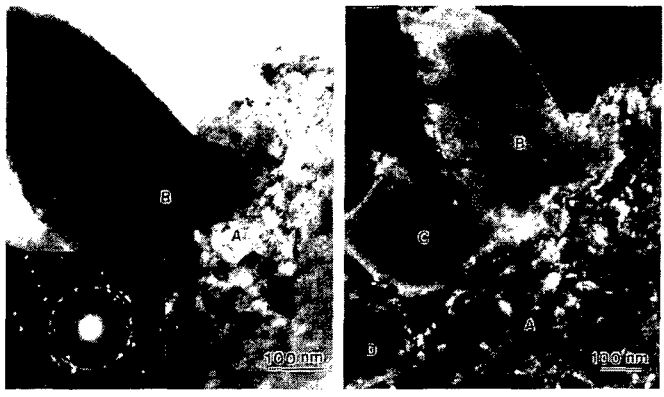

Figure 3. TEM micrograph of metallurgical agglomeration powders: (a) bright field image and (b) dark field image.

The average sizes of self-agglomerates and particles are shown in Figure 4. In the powder milled for two hours there is no evidence of self-agglomeration. However, in the powder milled for four hours a large portion of the smaller particles self-agglomerate; the larger carbide particles remain segregated. In an individual powder system, the size of the binder-induced agglomeration powder is thought to depend on the dynamic factors in the milling process, such as rotation, ball to

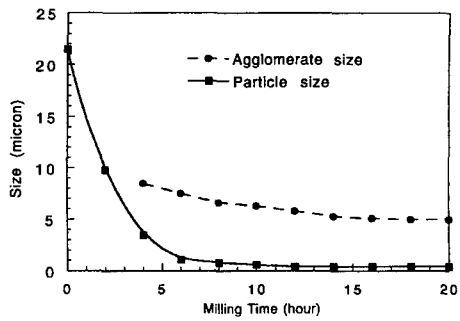

Figure 4. Variation of average sizes of agglomerate and particle.

powder mass ratio, tank dimensions, and the behavior of the milling media used. Dry inert gas, air, liquid nitrogen, liquid chemicals (such as Methanol, Acetone and Hexane) are often used as milling media. The behavior of the milling media affects the size of the agglomerates. In special case, binder chemicals are often added into the powder to change behavior of the binder-induced agglomeration. However, a systematic study on the binder-induced agglomeration is currently unavailable. Under the present conditions, the size of the binder-induced agglomeration particles approaches a constant value of 5 micron after 8 hours of milling. Interestingly, the particle size also approaches a constant value of 0.5 micron. The fact that the average particle size approaches a constant value is an indication that the smaller particles grow while the larger particles fracture. Benjamin [16] introduced an assumption to explain the stabilization of the average particle size. Fracture strain of particles decreased with increasing particle size, while the strain value at which cold welding occurred was constant, hence, average the particle size tended to stabilize as milling time increased. Apparently, both fracture and weld strains depend strongly on powder characteristics and milling conditions. In related studies, it was reported that the average powder size of Ni-based superalloys, containing a small amount of Y_2O_3, increased and approached a constant value of between 110 and 130 microns as milling progressed [16]. Brittle powder systems, such as the present 75% Cr_3C_2-25% Ni20Cr system, possess low fracture strain, therefore, the average particle size approaches a constant value on the order of 1 micron. By contrast, a continuous decrease in powder size for both ductile-ductile (Ti-Al) and ductile-brittle (Ti-Si) systems [22] occurred with increasing milling time. Lau *et al.* [14] indicated that the milling media affected the dependence of average powder size versus milling times of Ni powders. As milling time increased, Ni powder size decreased when milled in Methanol, whereas the powder size increased when milled in liquid nitrogen. Due to a number of changeable experimental parameters, it is difficult to estimate an average size of milled powder.

2.3. STRUCTURAL AND CHEMICAL COMPOSITION CHANGES OF THE POWDERS DURING MILLING

X-ray diffraction (XRD) spectrums of the powders following different milling times are shown in Figure 5. Figure 5 (a) indicates that as-received Cr_3C_2-NiCr powder consists of the Cr_3C_2 carbide phase and a NiCr solid solution. The Cr_7C_3 carbide phase can not be simply identified by this XRD spectrum because all the diffraction peaks from Cr_7C_3 carbide overlap those from Cr_3C_2 carbide or the NiCr solid solution. Guilemany and Calero [23] analyzed commercial Cr_3C_2-NiCr powder by EPMA and distinguished three phases, mainly Cr_3C_2, some Cr_7C_3, and NiCr solid solution. These three phases were identified by the presence of three regions with distinct chemical composition.

Ni20Cr solid solution has a f.c.c. structure with lattice constant of a=0.35454 nm, while the lattice constant of pure Ni crystal is 0. 35238 nm, based on JCPDS file provided by International Centre for Diffraction Data [PDF#04-0850]. The substitution of Cr for 20% Ni leads to 0.6% increase in lattice constant. Cr_3C_2 and Cr_7C_3 carbides are well documented in JCPDS files. They have orthorhombic and hexagonal crystal structures, respectively.

With increasing milling time, XRD peaks from NiCr solid solution show a larger change compared with those from Cr_3C_2 carbide. The XRD peaks broaden and decrease

drastically, then nearly disappear in the powder following 16 hours of milling. This indicates that there is a larger change in the structure of NiCr solid solution powder than in Cr_3C_2 carbide. During milling, the NiCr solid solution powder, with lower hardness, is subjected to double milling from both the stainless steel balls and the hard chromium carbide particles. Hence, the NiCr solid solution powder undergoes more severe plastic deformation. The intensity of the strongest diffraction peak, which is located at the position of $2\theta=19.96^{\circ}$ and belongs to both NiCr solid solution and Cr_7C_3 carbide, decreases in comparison with the diffraction peaks of Cr_3C_2. The peak does not disappear in the powder milled for 16 hours. This confirms a heavier deformation in NiCr powder and the presence of Cr_7C_3 carbide in the system.

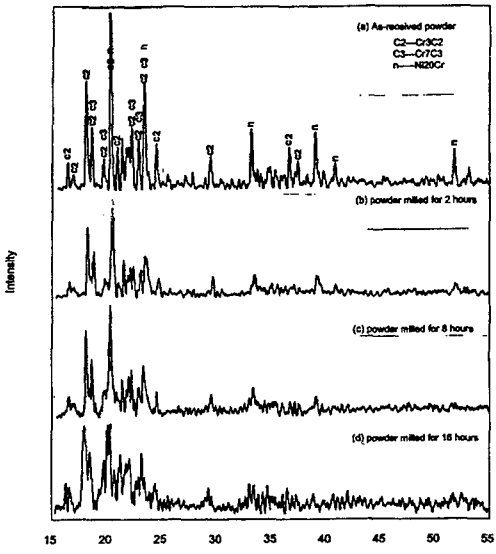

Figure 5. X-ray diffraction spectrums of the powders. Following different milling times.

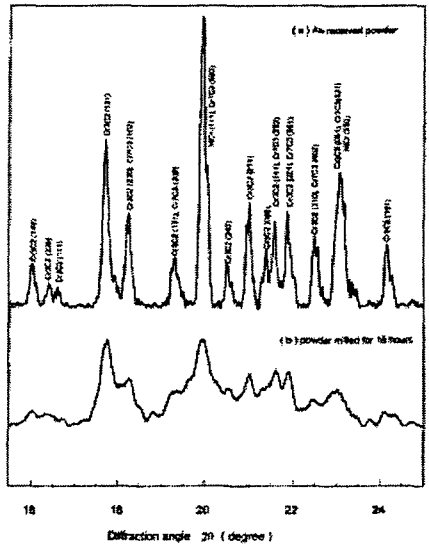

Figure 6. Detailed view of XRD spectrums.

Hard and brittle chromium carbides fracture during milling. Figure 6 shows detailed views of XRD spectrums between the diffraction angle (2θ) range of 15 to 25 degrees for the as-received powder and the same powder milled for 16 hours. The diffraction peaks from the milled powder broaden noticeably. The grain sizes of the milled powders following different milling times are determined on the basis of the Scherrer equation [24], and the results are plotted in Figure 7.

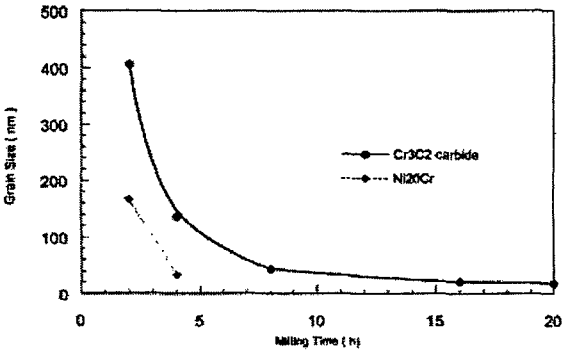

Figure 7. Dependence of grain sizes on milling time.

Grain size of Cr_3C_2 carbide ranges from 406 nm in the powder milled for 2 hours down to 17 nm in the powder milled for 20 hours. Grain sizes of the NiCr solid solution milled for 2 and 4 hours are calculated to be 166 and 33 nm, respectively. It is not possible to determine the grain size of the NiCr solid solution for longer milling times because the individual diffraction peaks from the NiCr solid solution cannot be differentiated for milling times in excess of 6 hours. The grain size of Cr_7C_3 carbide can not be measured by X-ray because there is no separation between Cr_7C_3 carbide diffraction peaks in the XRD spectrum. However, it may be reasonably assumed that the grain size of Cr_7C_3 carbide in the powder milled for 20 hours is smaller than 50 nm because the grain sizes of Cr_3C_2 carbide and NiCr solid solutions are less than 50 nm.

Contamination is unavoidable during the milling process. To profile the contamination extent under Hexane [$H_3C(CH_2)_4CH_3$] milling, the changes of chemical composition with milling times are listed in Table 1. According to Table 1, as milling time increases, the percentage of carbon decreases while the percentage of nitrogen and oxygen increases. This indicates that decarburization and contamination occur during milling. However, no new peaks appear in the X-ray spectrum of the milled powder, proving that the amount of contaminants is less than the minimum limit (around 5%) which X-ray diffraction can detect. In related studies, nitride and oxide phases in nanostructured materials played a beneficial role in retarding grain growth [25-26].

Table 1. Dependence of chemical composition on milling time (wt. %)

Milling time (h)	Cr	Ni	C	N	O
0	70.0	19.2	9.83	0.20	0.21
8	66.2	19.7	9.71	0.38	1.11
20	64.3	18.8	9.36	0.51	1.93

2.4. MILLING MECHANISM OF Cr_3C_2-NiCr

Figure 8 (a) shows a bright field consisting primarily of the NiCr solid solution in the 2 hour milled powder, and Figure 8 (b) and (c) are the corresponding selected area diffraction (SAD) patterns of powders A and B in Figure (a). Based on the SAD patterns, powder A is nearly a single crystal of NiCr solid solution although a few fragments from other powders can be seen. Carbide particles can be identified as being embedded into powder B because ambiguous diffraction rings overlap the SAD pattern of single crystal NiCr solid solution. With increasing milling time, more carbide

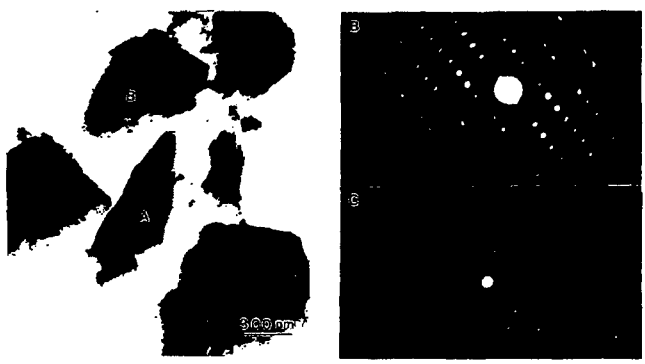

Figure 8. TEM image of NiCr solid solution in the 2 hour milled powder: (a) bright field micrograph; (b) SAD pattern of powder A and (c) SAD pattern of powder B.

particles are embedded into the NiCr solid solution. Figure 9 (a) displays a bright field image of the 4 hour milled powder, and Figure 9 (b) shows the corresponding dark field image, using a carbide diffraction spot, in which many carbide particles can be seen. In this figure, clearer carbide diffraction rings, which overlap the SAD pattern of single crystal NiCr solid solution, can be seen.

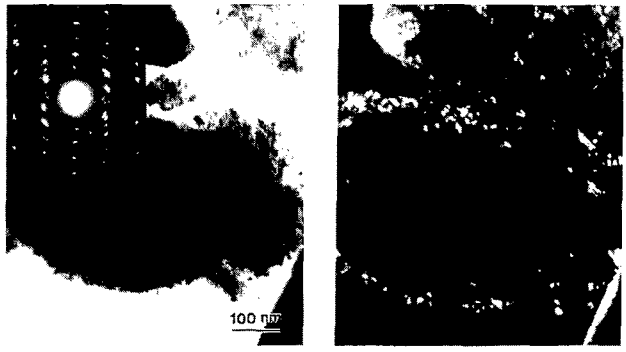

(a) (b)

Figure 9. Micrograph of the powder following 4 hours of milling: (a) bright field; (b) dark field image.

Figure 10 shows that a carbide powder, in the 8-hour milled powder, fractures into a number of fragments that are embedded into the NiCr solid solution. It can be verified that the carbide and binder metal combine into a polycrystal nanocomposite powder because the SAD pattern is made completely of diffraction rings. The carbide fragments in the polycrystal nanocomposite have a sharp shape. Figure 11 (a) and (b) display a bright field and the corresponding dark field image of a polycrystal nanocomposite powder after 20 hours of milling. Large proportions of carbide fragments have transformed into round carbide particles. The average size of these round carbide particles was approximately 15 nm, which agrees with the X-ray measurements. Apparently, the

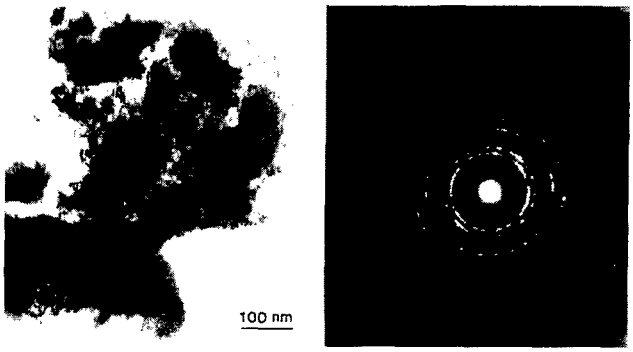

(a) (b)

Figure 10. Carbide fragments in the powder milled for 8 hours: (a) bright field image; (b) SAD pattern.

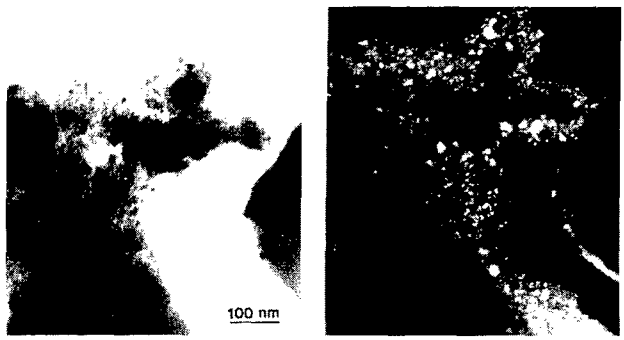

(a) (b)

Figure 11. Polycrystal nanocomposite Cr_3C_2-NiCr powder: (a) bright field image; (b) dark field image.

micrograph and SAD patterns shown in Figures 8 through 10 exhibit transition microstructures of the powders during milling. The milled powders are found to continually overlap, cold weld, fracture, and gradually transform into polycrystal nanocomposites, in which round nanostructured carbide particles are uniformly distributed. The milling mechanism is schematically shown in Figure 12.

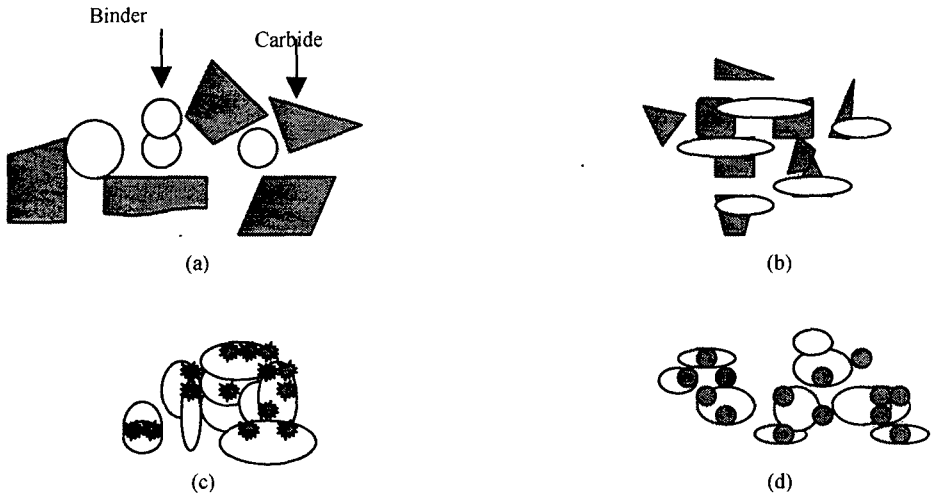

Figure 12. Schematic of milling mechanism for duplex structure powder: (a) Initial stage; (b) NiCr overlap and deform, Cr_3C_2 fracture and embed into NiCr; (c) Binders deform, fracture, and weld, carbide fracture further; (d) Nanocomposite powder.

3. Thermal Spraying of Nanocomposite Powder

Nanostructured and conventional Cr_3C_2-NiCr (Dialloy 3004 blended Cr_3C_2-25 (Ni20Cr), with a nominal particle size of (-45+5.5) μm, produced by Sulzer Metco (US) Inc.) powders were used for spraying using HVOF.

3.1 AGGLOMERATION

The thermal spray process typically requires a powder size within the range of 10-50 μm. The as-synthesized nanostructured Cr_3C_2-NiCr powder is approximately 5 μm and hence not suitable for thermal spraying in the as-synthesized condition. Accordingly, a procedure was established for the agglomeration of the Cr_3C_2-NiCr powder into larger-sized particles. Using a 2% methyl cellulose solution in H_2O, the powder is made into a slurry. This slurry was annealed in a vacuum furnace at a temperature of 80°C for a time period ranging from 24 to 48 hours. The annealing time is a function of the quantity of the slurry to be baked. As a result of the annealing, a solid block of material was formed. This block is relatively brittle and can easily be crushed into powder. This powder was then sieved through a sub-50 μm mesh. The resulting powder was found to have an adequate particle size (approximately 40 μm) to flow in the HVOF system used.

3.2 HVOF THERMAL SPRAY PROCESS

To spray the Cr_3C_2-NiCr coatings, a Sulzer Metco Diamond Jet HVOF thermal spray facility is used. As shown in Figure 13, the Diamond Jet brings in oxygen, air and fuel, in this experiment propylene, from the DJC into the rear of the gun in the proper stoichiometric ratios. This gaseous mixture is ignited by an arc current creating a hypersonic, low temperature flame with gas velocities of 1830m/s and temperatures around 2700 K. From the 9-MP hopper powder feed unit, nitrogen carrier gas brings the agglomerated powder into the rear of the gun and then axially into the flame. The powder is heated in the gun barrel then sprayed out onto a stainless steel substrate. The spraying parameters are summarized in Table 2.

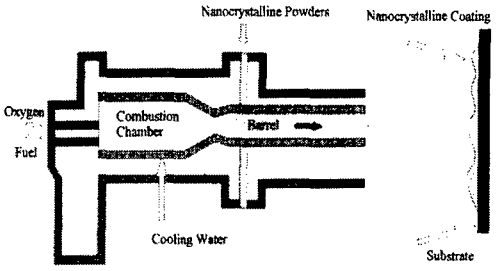

Figure 13. Schematic of HVOF process

Table 2 Spraying parameters used to produce Cr_3C_2-25(Ni20Cr) coatings

Gas	Pressure(psi)	FMR*	SCFH**	Parameter	Setting
Air	100	48	857	Powder feed rate	2.5 lbs/hr
Fuel	100	40	176	X-Y traverse speed	200 ft/min
Nitrogen	150	55	28	Spraying distance	9 in
Oxygen	150	40	578		

FMR: flow meter reading; **SCFH: standard cubic feet/hour.

4. Coating Characterization

The cross-sections of the coatings are examined using Philips XL 30 FEG SEM. The microhardness is tested on a Buehler Micromet 2004 Microhardness tester using a load of 300 gram. Each microhardness value is obtained from an average value of 30 tests. After removal of the substrate by polishing, the TEM specimens are prepared by cutting out a section of the coating and forming 3-mm diameter disks. The disks are dimpled to around 30 μm thick using a dimpler fitted with diamond grinders. The grinding size descends from 6 μm grade, down to 3 μm, and finally to 1 μm grade. The final thinning perforation process is performed using an argon ion miller. With the prepared samples, TEM observation is carried out on the Philips CM20 microscope operated at 200 keV.

4.1. MICROSTRUCTURE OF COATINGS

The microstructures of conventional and nanostructured Cr_3C_2-NiCr coatings, examined using SEM, are shown in Figure 14. A uniform and dense microstructure is observed in the nanostructured coatings, compared to the conventional Cr_3C_2-NiCr coating which is observed to have an inhomogeneous microstructure. Five carbide (dark phase) and

binder areas (bright phase) are randomly chosen for SEM EDS analysis of their chemical composition. The results of this analysis are listed in Table 3. The distributions of Cr and Ni in carbide particle and binder phase are obtained from the average value of 5 readings. The row labeled "average" in Table 3 is obtained from low magnification analysis (A number of carbide phasees and binder phases are enclosed) and is also the average value of 5 readings.

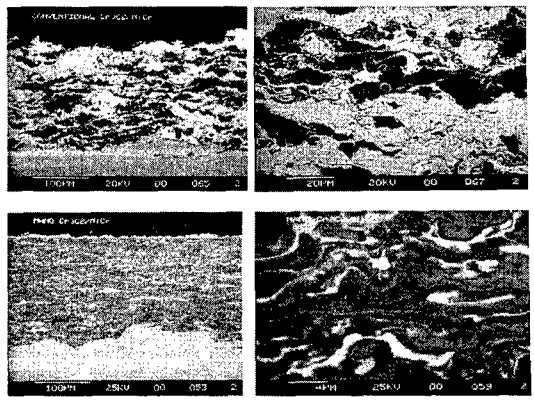

Figure 14. Microstructure of Cr_3C_2-25(Ni20Cr): (a) conventional coating; (b) magnification of (a); (c) nanostructured coating and (d) magnification of (c).

Table 3 Chemical composition of Cr_3C_2-25(Ni20Cr) coatings (wt %)

	Conventional coating		Nanostructured coating	
	Cr	Ni	Cr	Ni
Average	46.3	53.7	76.25	23.75
Binder	16.21	83.79	31.12	68.88
Carbide	99.15	0.85	94.34	5.66

In the binder phase of the conventional coating, the contents of Cr and Ni are close to the nominal chemical composition of pure NiCr solid solution (80% Ni and 20% Cr), thus the binder phase is considered to be the NiCr solid solution phase. A minor amount of Ni exists (0.85%) in the carbide phase. For the nanostructured coating, a higher Cr content in the binder phase and a higher Ni content in the carbide phase are observed. During milling, carbide particles are fractured and embedded into binder phases. Thus the most of binder phases combine with fractured carbide particles to form nanocomposite, and a relatively small amount of binder phases are still present in the nanocomposite feedstock powder. However, the binder phases are not completely pure NiCr solid solution, which contains more or less carbide particles. This causes a higher Cr content in the binder phases within the nanostructured coating. Similarly, binder phases are present in gaps between fractured carbide particles in the nanocomposite feedstock powder, thus Ni is observed in the carbide phase of the nanostructured coating. In addition to, the measurement of elements in individual phase of the nanostructured coating is partly affected by the beam size limitations of the EDS. Since both the binder phase and carbide phase are extremely fine in the nanostructured coating, a pure binder phase area or carbide phase area can not be perfectly isolated for SEM EDS analysis. Thus, the constituents of the binder phase in the nanostructured coating likely include a carbide phase, or *vice versa.*

To compare the average chemical composition (labeled "average" in Table 3) of the

coatings with those of the feedstock powders listed in Table 1, a simple correction for data in Table 3 is made because the light elements, such as C, N, and O, are not included in the EDS analysis. In Table 3, the sum of Cr and Ni content is 100%. Actually, the sum of Cr and Ni content is 89.2 % in the conventional feedstock powder, and 83.1% in the nanocomposite feedstock powder, see Table 1. Therefore, the content of Cr and Ni is multiplied by factors of 0.892 in the conventional coating, and 0.831 in the nanostructured coating. This correction represents a simple approximation because it implies that there are no changes in the contents of all elements during thermal spraying, whereas in practice, this may not be the case. After making this simple correction, the average contents of Cr and Ni are 41.3% and 47.9% in the conventional coating, and 63.4% and 19.8% in the nanostructured coating, respectively. It is worth noting that there is a large average chemical composition difference between the conventional and nanostructured coatings. The average contents of Cr and Ni in the nanostructured coatings are close to those of feedstock nanocomposite powder. However, those same values found for the conventional coating differ markedly from the conventional feedstock powder. Because the contents of Ni and Cr in both the binder and the carbide phase are close to their nominal contents, the chemical composition difference between the conventional coating and feedstock powder is attributed to a decrease in the volume fraction of the carbide phase in the conventional coating. In related studies, the decarburization of tungsten carbide is widely reported [27-28], whereas chromium carbide is quite stable during thermal spraying [23]. Therefore, the measured decrease in the volume fraction of the carbide phase in the conventional coating may not be attributed to decarburization or oxidation of chromium carbide. Individual, large-sized regularly shaped carbide particles and spherically shaped binder phase particles are present in blended Cr_3C_2-NiCr powder. During spraying, the large-sized carbide particles, with a high melting point of 2200 K (T_l), may remain solid or semi-molten in the HVOF system (short dwell time and low temperature flame), yielding low adherence with the substrate surface. Conversely, melt binder phase droplets (melting point is 1690 K) have a more fluid characteristic than the carbide particles. The greater fluidity can result in effective contact of binder phase with the substrate surface. Thus, the volume fraction of the carbide phase decreases in the conventional coatings as a fraction of the carbide particles fail to adhere, and simply bounce-of from the substrate. In the case of the nanocomposite feedstock powder, there is high probability that the nanoscale carbide particles will be completely surrounded by the binder phase, as a result of their extremely small size (15 nm). The nanoscale particles are therefore co-coated with the binder phase and effectively adhere onto the substrate surface. Thus the improved fluidity leads to the nanostructured coating to have a close composition to the feedstock powder. Current efforts are aimed at providing quantitative support to this suggestion via studies of carbide particle size distribution during milling.

The commercially available blended Cr_3C_2-NiCr powders are mixtures of Cr_3C_2 and NiCr solid solution and these mixtures are inherently difficult to handle because of segregation during storage, transportation and spraying [29, 30]. Consequently, these mixtures usually produce an inhomogeneous microstructure characteristic [29, 30]. In this study, the decrease in the volume fraction of the carbide phase in the conventional coating is an indicative of a non-uniformity in the microstructure. Coating performance is known to be very susceptible to the non-uniformity of microstructure [29-31]. A few

pre-treatment methods have been developed to overcome these types of microstructural variations. Two such methods, referred to as "pre-alloying" [30] and "cladding" [29], are widely used. Using the "pre-alloying" method, the powders are first agglomerated using an organic polymeric binder and then heated and pre-sintered in hydrogen. The powders are then densified using a plasma flame in an inert atmosphere, and are finally milled, screened and classified to yield the desired particle size. In related study [30], the hardness of a plasma-sprayed Cr_3C_2-NiCr coating, using the "pre-alloyed" powder, increased from 594 to 796 DPH_{300}. In the "cladding" method, each Cr_3C_2 carbide particle is clad with an essentially continuous layer of NiCr solid solution; therefore, the Cr_3C_2 carbide is present as a discrete second phase particle randomly embedded in a NiCr solid solution. In related work [29], the hardness of a plasma-sprayed Cr_3C_2-NiCr coating increased from 620 to 860 DPH_{300}, and the wear resistance was also improved as compared to the standard blend coating method, presumably as a result of the uniform "clad" powder [29]. Using a Metco Diamond Jet system, Sasaki *et al.* [31] compared the behavior of HVOF thermally sprayed coatings made using four different types of Cr_3C_2-NiCr feedstock powders (blend, agglomerated/sintered, sintered/crushed and sintered/crushed/clad). They found that the coating made of the sintered/crushed/clad powder showed the best characteristics as compared with those coatings sprayed by other three types of powders. Therefore, regardless of the spraying method employed, the uniformity of microstructure in a coating has a significant positive influence on its performance.

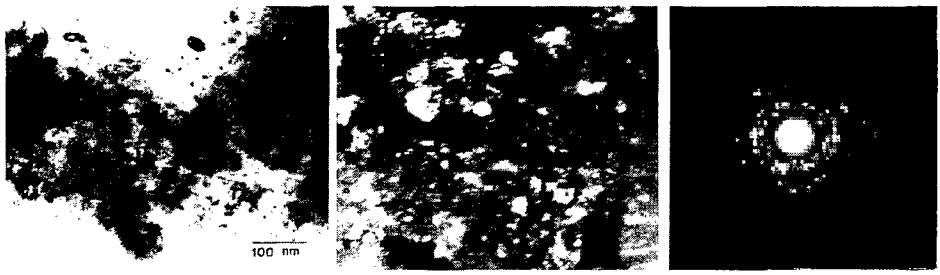

(a) (b) (c)

Figure 15. TEM observation of nanostructured Cr_3C_2-25(Ni20Cr) coating: (a) bright field, (b) dark field and (c) diffraction pattern.

In the present study, the Cr_3C_2-NiCr nanocomposite powder is synthesized using mechanical milling and agglomeration following the milling process. In this approach, the carbides in the nanocomposite powder are uniformly distributed in the NiCr solid solution. In essence, our approach yields a "clad" powder and hence a uniform microstructure is obtained in the nanostructured coating. In other words, the synthesis method of nanocomposite feedstock powder used in the present study provides a beneficial role in the uniformity of microstructure of the coatings.

The TEM bright field image of the nanostructured coating, the corresponding dark field image and diffraction pattern are shown in Figure 15 (a), (b) and (c), respectively. The average carbide particle size is approximately 24 nm. This indicates that the coating has a nanostructured microstructure. In the nanostructured WC-12%Co coating [20], TEM examination revealed a microstructure consisting of nano sized WC carbide

particles in an amorphous matrix phase. While in the nanostructured Cr_3C_2-NiCr coatings, the diffraction pattern does not exhibit clearly the presence of an amorphous matrix phase. Guilemany and Calero [23] also observed amorphous matrix phases in a conventional HVOF thermally sprayed Cr_3C_2-NiCr coating. Instead of an amorphous matrix phase, a few discontinuous elongated amorphous phases are observed in the nanostructured Cr_3C_2-NiCr coating, shown in Figure 16 (a) and (b). The inserted diffraction patterns, which are from the elongated phases marked A, show diffuse rings. Many fine diffraction spots are sharply imaged in the diffraction patterns, this indicates that the diffraction patterns are well focused. The diffuse rings are thus indicative of an amorphous phase rather than a false appearance caused by under/over focusing. These elongated amorphous phases, which have dimensions of around 100 nm wide and 1 μm long, are discontinuously distributed in the coating.

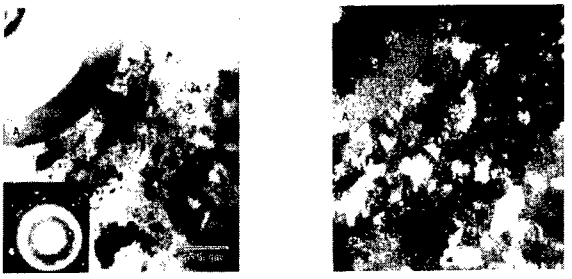

(a) (b)

Figure 16. Elongated amorphous phase in nanostructured $Cr_3C_2$25(Ni20Cr) coating: (a) bright field and (b) dark field.

4.2 MICROHARDNESS

The average microhardness of the nanostructured Cr_3C_2-NiCr coating, taken on the cross-section, increases from a value of 846 for the conventional Cr_3C_2-NiCr coating to 1020 DPH_{300} for the nanostructured coating. Hence nanostructured coating exhibits to a 20.5 % increase in microhardness as compared with the corresponding conventional coating. Several published hardness values of Cr_3C_2-NiCr coatings are listed in Table 4. The spraying methodology and the type of feedstock powder used (blend, agglomeration or clad) have very a significant influence on the hardness of coatings on the basis of the data in Table 4. Effects of spraying method [32, 33] and type of feedstock powder [28-31] on hardness has been extensively investigated. HVOF is characterized by high particle velocity and low thermal energy, this combination of high kinetic energy and low thermal energy leads to a high hardness [27]. The clad feedstock powders produce uniform Cr_3C_2-NiCr coatings and hence high hardness [29, 31]. It has been reported that the hardness of nanostructured materials often exhibits a 2-5 fold increase compared with that of the conventional materials although it is lower than that predicted using the classical Hall-Petch equation [34-36]. In a related study, Kear and McCandlish [37] also indicated that nanostructured WC-23%Co coatings have a higher hardness than that of the conventional coating of the same composition. Therefore, the high hardness of the nanostructured Cr_3C_2-NiCr coatings results primarily from two aspects: (1) uniformity of microstructure, caused by the synthesis process of nanocomposite feedstock powder; and (2) the intrinsically high hardness of nanostructured materials.

Table 4 Published hardness data of Cr_3C_2-25(Ni20Cr) coatings

Spraying method	Powder	Hardness	Source
High Velocity Oxygen Fuel	Commercial	855 (HV_{300})	[38]
High Velocity Oxygen Fuel	Commercial (sintered/crushed/clad)	950 (DPH_{300})	[31]
High Velocity Oxygen Fuel	Commercial (blend)	700 (DPH_{300})	[31]
High Velocity Oxygen Fuel	Commercial (agglomeration)	914 (DPH_{300})	[28]
High Velocity Oxygen Fuel	Commercial (blend)	697(DPH_{300})	[28]
Detonation gun spraying	Commercial (powder size: 10-44 μm)	800 (HV_{300})	[39]
Atmospheric Plasma Spraying, Ar/H_2	Commercial	830(HV_{300})	[32]
Atmospheric Plasma Spraying, Ar/He	Commercial	871(HV_{300})	[32]
Continuous detonation spraying	Commercial	828(HV_{300})	[32]
Atmospheric Plasma Spraying, Ar/H_2	Commercial	837(HV_{300})	[33]
Atmospheric Plasma Spraying, Ar/He	Commercial	943 (HV_{300})	[33]
Continuous detonation spraying	Commercial	889 (HV_{300})	[33]
Detonation gun spraying	Commercial	945 (HV_{300})	[33]
High Velocity Oxygen Fuel	Commercial (blend)	846 (DPH_{300})	This study
High Velocity Oxygen Fuel	Nanostructured	1020 (DPH_{300})	This study

The abrasion resistance of thermal sprayed coatings is significantly related to the relative fracture toughness [40]. The indentation fracture method is often employed to characterize the relative fracture toughness of coatings [40]. In this study, an indentation fracture examination is performed and the results are shown in Figure 17 (a) to (d). Under the same load, indentation marks in the nanostructured coating are smaller than those in the conventional coating because the nanostructured coating has a higher hardness. Under a load of 1000 grams, many cracks caused by an indentation along the phase interface of carbide phase with metal binder phase are observed in the conventional coating, and some cracks are also found in the nanostructured

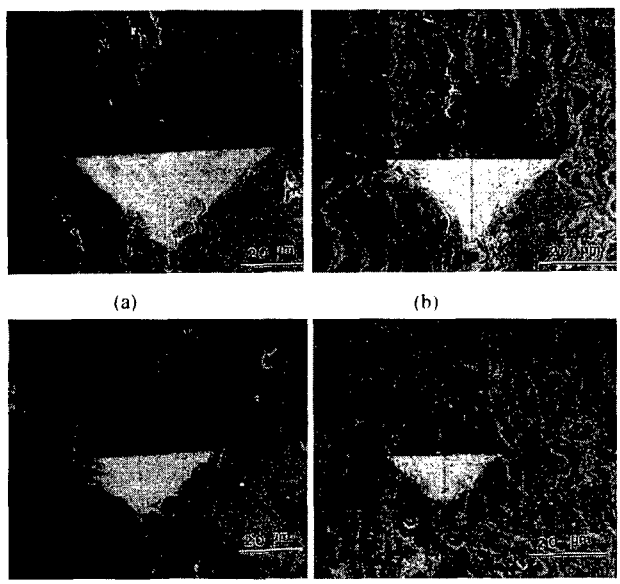

Figure 17. Indentation cracking: (a) conventional coating at 1000 grams; (b) nanostructured coating at 1000 grams; (c) conventional coating at 500 grams and (d) nanostructured coating at 500 grams.

coating. When the load is decreased to 500 grams, a few cracks around the indentation are still observed in the conventional coating, whereas none are present in the nanostructured coating. These results suggest that the nanostructured Cr_3C_2-NiCr coating possesses a higher apparent fracture toughness relative to that of the conventional material. Further work in this area is continuing in an effort to provide more insight into the fracture behavior of nanostructured coatings.

5. Summary

In this paper, the synthesis of nanocomposite coatings is described in detail as related to: (1) synthesis of nanocomposite feedstock powder; (2) characteristics of milled powder; (3) milling mechanism of a duplex structure powder; (4) thermal spraying process of nanocomposite coatings and (5) microstructures and properties of nanocomposite coatings.

6. Acknowledgments

The authors gratefully acknowledge financial support provided by the Office of Naval Research (Grants No.: N00014-94-1-0017, N00014-97-1-0844 and N00014-98-1-0569).

7. Reference

1. Pawlowski, L (1995) *The Science and Engineering of Thermal Spray Coatings*, John Wiley & Sons. England.
2. Roseberry, T. J. and Boulger, F. W. *A plasma flame spray handbook, U. S. Department of Commerce Report No. MT-043*, National Technical Information Service, Springfield, VA.
3. Lavernia, E. J., Lau, M. L. and Jiang, H. G. (1998) Thermal spray processing of nanocrystalline materials, in G. M. Chow and N. I. Noskova (eds.), *Nanostructured Materials*, Kluwer Academic Publishers, Dordrecht, The Netherlands, pp. 283-302.
4. Eidelman, S. and Yang, X. (1997) *NanoStructured Materials*, **79**, 9.
5. Sobolev, V.V. and Guilemany, M. (1996) *Int. Mat. Rev.*, **41** (1), 13.
6. Knotek, O. and Schnaut, U. (1992) Process modeling of HVOF thermal spraying systems, in C. C. Berndt (ed), *Thermal Spray: International Advances in Coatings Technology*, ASM International, Materials Park, Ohio, pp. 811-816.
7. Parker, D. W. and Kutner, G. L. (1991) *Adv. Mat. Process* **139**, 68.
8. Varacalle, D. J., Ortiz, M. G., Miller, C. S., Steeper, T. J., Rotolico, A. J., Nerz, J. and Riggs (II), W. L. (1992) HVOF combustion spraying of Inconel powder, in C. C. Berndt (ed), *Thermal Spray: International Advances in Coatings Technology*, ASM International, Materials Park, Ohio, pp. 181-187.
9. Srivatsan, T.S. and Lavernia, E. J. (1992) Review-Use of spray techniques to synthesize particulate-reinfored metal-matrix composites, *J. Mat. Sci.* **27**, 5965.
10. Apelian, D., Wei, D. and Farouk, B. (1989) *Metall. Trans.* **20B**, 251.
11. Hackett, C. M. and Settles, G. S.(1996) in C. C. Berndt (ed), *Thermal Spray: Practical Solutions for Engineering Problems*, Materials Park, Ohio, p665.
12. Birringer, R. (1994) in G. C. Hadjipanayis and R. W. Siegel (eds.), *Nanophase Materials: Synthesis-Properties-Applications*, Kluwer Academic Publishers, Dordrecht, The Netherlands, p.157.
13. Birringer, R. (1989) *Mat. Sci. & Engr.*, **A117**, pp. 33.
14. Lau, M. L., Jiang, H. G., Nuchter, W., and Lavernia, E. J. (1998) *Phys. Stat. Sol. (a)*, **166**, pp. 257.
15. Suryanarayana, C. (1995) Nanocrystalline materials, *Int. Mat. Rev.* **40**, 41.
16. Benjamin, J. S. (1992) Fundamentals of mechanical alloying, in P. H. Shingu (ed), *Mechanical Alloying* (Mater. Sci. Forum, Vol. 88-89), Trans Tech Publications, Switzerland, pp.1-17.
17. Koch, C. C.(1992) The synthesis of non-equilibrium structures by ball-milling, in P. H. Shingu (ed), *Mechanical Alloying* (Mater. Sci. Forum, Vol. 88-89), Trans Tech Publications, Switzerland, pp.243-262.
18. Jang, J. S. C. and Koch, C. C. (1990), J. Mat. Res., **5**, 498.

19. He, J., Ice, M. and Lavernia, E. J. (1998) Synthesis and characterization of nanostructured Cr_3C_2-NiCr, *NanoStructured Materials*, **10**, 1271.
20. He, J., Ice, M. and Lavernia, E. J. (1999) Synthesis of nanostructured WC-12%Co coating using mechanical milling and HVOF thermal spraying, submitted to *Metall. Trans.*
21. He, J., Ice, M. and Lavernia, E. J. (1999) Synthesis of nanostructured Cr3C2-25(NiCr) coatings, submitted to *Metall. Trans.*
22. Ahn, J. H., Chung, H.S., Watanabe, R. and Park, Y.H. (1992) Microstructural refinement & amorphization in Ti-Al, Ti-Si and Si-W system by mechanical alloying, in P. H. Shingu (ed), *Mechanical Alloying* (Mater. Sci. Forum, Vol. 88-89), Trans Tech Publications, Switzerland, pp.347-354.
23. Guilemany, J. M. and Calero, J. A. (1997) Structural characterization of chromium carbide-nickel chromium coatings obtained by HVOF spraying, in C. C. Berndt (ed.), *Thermal Spray: A United Forum for Scientific and Technological Advances*, ASM, Materials Park, Ohio, pp. 717-721.
24. Gullity, B. D.(1978) *Elements of X-ray Diffraction*, Addison-Wesley, Reading, MA(1978).
25. Luton, M.J., Jayanth, C.S., Disko, M.M., Matras, S. and Vallone, J. (1989) *Mater. Res. Soc. Proc.*, **132**, 79.
26. Lau, M.L, Huang, H., Perez, R.J., Juarez-Islas, J. and Lavernia, E.J. (1996), *NanoStruct. Mater.* **7**, 847.
27. Vuoristo, P., Niemi, K., Mantyla, T., Berger, L.M. and Nebelung, M. (1995) Comparison of different hard, metal like coatings sprayed by plasma and detonation gun processess, in C. C. Berndt and S. Sampath(eds.), *Thermal Spray Science & Technology*, ASM International, 1995, pp. 309-315.
28. Russo, L. and Dorfmann, M. (1995) A structural evaluation of HVOF sprayed NiCr-Cr_3C_2 coatings, in A. Ohmori (ed.), *Thermal Spraying: Current Status and Future Trends*, High Temperature Society of Japan, 1995, pp. 681-686.
29. Reardon, J. D., Mignogna, R.. and Longo, F. N.. (1981) Plasma and vacuum plasma-sprayed Cr_3C_2 composite coatings, *Thin Solid Films*, **83**, 345-351.
30. Houck, D. L. and Chency, R. F. (1984) Comparison of properties of Cr3C2-NiCr coating thermally sprayed from pre-alloyed and mechanical mixed powders, *Thin Solid Films*, **118**, 507-513.
31. Sasaki, M., Kawakami, F., Komaki, C. and Ishida, M.(1992) Characterization of HVOF sprayed Cr_3C_2 coating, in C. C. Berndt (ed.), *Thermal Spray: International Advances in Coatings Technology*, ASM International, pp. 165-170.
32. Vuoristo, P., Niemi, K., Makela, A. and Mantyla, T. (1994) abrasion and erosion wear resistance of Cr_3C_2-NiCr coatings prepared by plasma, detonation and HVOF spraying, in C. C. Berndt and S. Sampath (eds.) *Thermal Spray Industrial Applications*, ASM International, pp. 121-126.
33. Niemi, K., Vuoristo, P., Mantyla, T., Barbezat, G., and Nicoll, A. R. (1992) Abrasion wear resistance of carbide coatings deposited by plasma and high velocity combustion process, in C. C. Berndt (ed.) *Thermal Spray: International Advances in Coatings Technology*, ASM International, pp. 685-689.
34. Liu, X. D., Nagumo, M. and Umemoto, M. (1997) *Mater. Trans., JIM*, **38**, 1033-1039.
35. Suryanarayana, C., Mukhopadhyay, D., Patankar, S.N. and Froes, F. H.(1992) *J. Mater. Res.*, **7**, 2114-2117
36. D. A. Konstantinidis, D. A., and Aifantis, E. C. (1998) *NanoStructured Mater.*, **10**, 1111-1118.
37. Kear, B. H. and McCandlish, L. E. (1993) *Nanostructured Mater.*, **3**, 19-30.
38. Crawmer, D.C., Krebsbach, J. D. and Riggs, W. L.(1992) Coating development for HVOF process using design of experiments, in C. C. Berndt (ed.), *Thermal Spray: International Advances in Coatings Technology*, ASM International, pp. 127-136.
39. Fukuda, Y and Kumon, M. (1995) Application of high velocity flame sprayings for the heat exchanger tubes in coal fired boilers, in A. Ohmori (ed), *Thermal Spraying: Current Status and Future Trend*, High Temperature Society of Japan, pp. 107-111.
40. Usmani, S., Sampath, S. and Herman, H. (1998) in C. C. Berndt and E. J. Lavernia (eds.), *Thermal Spray Processing of Nanoscale Materials-A Conference Report with Extended Abstracts, J. of Thermal Spray Technol.*, **7**, p 429.